Nano Research

Open Access

Research Article

C-modified amorphous NiFe alloy nanoparticle via simple room temperature fermentation for efficient oxygen evolution reaction

Yanzhen Qiu[1], Lu Pan[1], Huimin Jiang[1], Mohammed A. Amin[2], and Jianjian Lin[1] ✉

[1] *Key Laboratory of Eco-chemical Engineering, College of Chemistry and Molecular Engineering, Qingdao University of Science and Technology, Qingdao 266042, China*
[2] *Department of Chemistry, College of Science, Taif University, P.O. Box 11099, Taif 21944, Saudi Arabia*

Cite this article: *Nano Research*, **2025**, *18*, 94907019. https://doi.org/10.26599/NR.2025.94907019

ABSTRACT: Amorphous alloys are promising candidates for oxygen evolution reaction (OER) applications due to their unique structural features, including abundant active sites, tunable chemical composition and high structural flexibility. However, there is a main challenge in the improvement of stability due to the short-range order structure of amorphous alloys. In this work, we synthesized C-modified amorphous NiFe alloy (C-NiFe(BP)) via a novel one-step annealing method with the introduction of glucose at room temperature fermentation. The as-prepared C-NiFe(BP) achieves an ultra-low overpotential of 219.7 mV and a Tafel slope of 43.17 mV·dec^{-1} at the current density of 10 mA·cm^{-2}, which surpass the reported amorphous NiFe (*a*-NiFe) based alloys in OER. X-ray diffraction (XRD) and X-ray photoelectron spectroscopy (XPS) analyses reveal that carbon modification widens the spacing between catalyst layers, exposing more active sites and promoting charge transfer between elements, thereby improving OER performance. Moreover, the C-NiFe(BP) exhibits promising stability during durability test for 20 h and cyclic voltammetry test for 1000 cycles. We discussed the influence of fermented glucose and indicated that the room temperature fermentation method can enhance the effect of carbon modification on catalyst activity, which further enhances the performance and stability of C-NiFe(BP) in OER. Combining common fermentation processes in life with scientific research to better enhance the performance of catalysts and improve scientific research methods. This work provides an innovative approach on the synthesis of stable C-modified *a*-NiFe alloy catalysts and further promotes the development of high-performance OER catalysts.

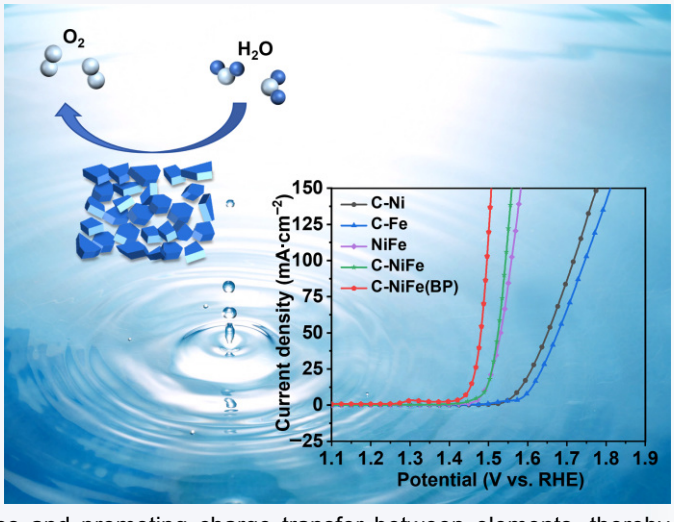

KEYWORDS: carbon modification, amorphous NiFe alloy, room temperature fermentation, oxygen evolution reaction

1 Introduction

Since the 20th century, hydrogen energy, as a green, sustainable and efficient energy source, has gradually become more prominent [1–3]. Among the many green hydrogen production technologies, water electrolysis is considered one of the most compelling energy conversion technologies due to its high efficiency in producing high purity hydrogen [4, 5]. This technology entails altering the redox potential of water through electrolysis, resulting in the production of O_2 and H_2 [6, 7]. The oxygen evolution reaction (OER) is the half reaction of water electrolysis. It requires a four-electron coupled transfer process with unfavourable reaction kinetics. The critical rate step limits the decomposition of water during the reaction [8, 9].

Therefore, researchers have implemented numerous tactics to enhance the reaction kinetics of OER. However, it should be noted that the overpotential of OER remains significantly high when compared to hydrogen evolution reaction (HER) [10–14]. Catalysts made from transition metals can effectively reduce the cost compared to precious metals. But the OER involves various

Received: July 8, 2024; **Revised:** August 27, 2024
Accepted: August 31, 2024

✉Address correspondence to Jianjian_Lin@qust.edu.cn

adsorption and desorption processes that are kinetically slow. The modulation of synergistic active sites on transition metal catalysts is an effective way for the improvement of OER performance and stability [15–19]. Among the various 3d-transition metal based nanocatalysts, nickel and iron show promising potential in catalytic activity and stability for OER in alkaline solutions [20, 21]. The synergistic effect of nickel- and iron-based binary alloys (NiFe) could modulate the electronic structure around the active site and the intrinsic high density, low coordination sites and good electrical conductivity could further improve the OER kinetics, which have attracted much attention in recent years [22–25]. For example, Moureaux et al. investigated a series of alloys with varying Fe-Ni atomic ratios and confirmed the spontaneous formation of a highly active NiFe oxo-hydroxide surface for efficient OER. This study reveals the nature of the active sites and the synergistic effect between Fe and Ni atoms [26]. Chen et al. synthesised Ni-Fe alloy nanocomposites using a heterometallic modified strategy, resulting in a centrosymmetric structure with good OER properties. This is the first time that NiFe alloy nanomaterials originated by NiFe Schiff base centrosymmetric cluster facilitates have been realised, providing a new blueprint for designing efficient OER electrocatalysts [27].

Amorphous alloys, as a distinct group of solid materials, are characterized with long-range disorder in atomic order, with short-range order limited to only a few atoms [28, 29]. In comparison to crystalline alloys, amorphous alloys exhibit a greater number of defects and vacancies, resulting in a higher concentration of dangling bonds that serve as active sites for electrochemical reactions [29, 30–32]. The good electrocatalytic activity of amorphous electrocatalysts is primarily attributed to two factors: (1) the amorphous morphology can achieve both surface-limited and volume-limited domain electrocatalysis, (2) amorphous alloys tend to be rich in defects, which leads to enhanced catalytic activity [33–38]. The synthesis of amorphous alloys has been extensively studied so far, for example, Li et al. prepared NiFe amorphous nanoreactor (NiFe-ANR) oxides as OER electrocatalysts via a mild autocatalytic reaction. The amorphous nature of NiFe-ANR helps to convert it into highly active hydroxyl and its many fine grain boundaries increase the active sites, obtaining excellent OER performance [39]. Liu et al. successfully prepared a novel core–shell $NiFe(OH)_x$/(Ni, Fe)Se_2 hetero-structured catalyst. This amorphous-crystalline structure contains a large number of unsaturated active sites, enabling both surface- and volume-limited catalytic reactions [16].

However, nickel-iron alloys are susceptible to erosion in highly concentrated alkaline electrolytes and exhibit instability at elevated overpotentials. Furthermore, NiFe alloy nanoparticles have been observed to aggregate during electrochemical testing, which reduces the number of accessible active sites and hinders mass transfer. It is therefore imperative to develop an effective method to optimise the OER activity and stability of NiFe alloys. To address these challenges, researchers have investigated a range of strategies to enhance the permeability properties of amorphous alloys, including heterostructure construction, modified heteroatom and morphological modulation. The use of C as a catalyst modification strategy allows for the regulation of catalyst size and the exposure of additional active sites, thereby promoting electron transfer and enhancing catalytic activity. Furthermore, it facilitates the acceleration of ion and electron transfer rates while simultaneously reducing the simultaneous reduction of nanoparticle aggregation. Furthermore, the incorporation of a carbon dopant helps to stabilise its crystal structure and improve its stability.

In this work, a C-modified amorphous NiFe catalyst (C-NiFe(BP)) was synthesized with the introduction of glucose under room temperature fermentation. The synthesized C-NiFe(BP) exhibits excellent performance with an ultra low overpotential of 219.7 mV at a current density of 10 $mA{\cdot}cm^{-2}$. The utilization of glucose as a carbon source improves the stability of the catalyst, while room temperature fermentation allows the exposure of more active sites, contributing to the improvement of OER performance. This work provides a solid theoretical and experimental basis for the field of amorphous alloy synthesis, which is beneficial to the optimization on the stability and OER performance and further contributes to the development of efficient OER catalysts.

2 Experimental section

2.1 Reagents

Nickel acetylacetonate ($Ni(acac)_2$, analytical reagent (AR)), iron acetylacetonate ($Fe(acac)_3$, AR) and potassium bromide (KBr, AR) were purchased from Shanghai Maclinson Technology Co., Ltd. and Nafion ($C_7F_{14}O_4$, 5 wt.%) was purchased from Shanghai Aladdin Biochemical Science and Technology Co., Ltd. Glucose ($C_6H_{12}O_6$) was purchased from Xilong Chemical Co., Ltd. and baking powder was supplied from Qingdao, Shandong. Anhydrous ethanol (C_2H_5OH, AR) was purchased from Shanghai National Pharmaceutical Co., Ltd. The reagents required for experiments are all analytically pure and can be used directly without additional purification.

2.2 Synthesis of amorphous NiFe with different molar ratios

The mixture of 720 mg KBr, $Ni(acac)_2$ and $Fe(acac)_3$ were grinded and dissolved in a mixed solution of 25 mL ethanol and 5 mL deionized water (DIW), where the ratio between Ni and Fe is set as 3:1, 3:2, 3:3 and 2:3. The obtained solution is stirred at room temperature until the the water is completely evaporated. The dried mixture was subsequently inserted into a muffle furnace and heated to 300 °C with a heating rate of 5 $°C{\cdot}min^{-1}$ for 12 h. The powder was cooled to ambient temperature and washed multiple times with ethanol and deionized water and finally the *a*-NiFe alloy catalyst was obtained.

2.3 Synthesis of C-NiFe(BP), C-NiFe, C-Ni and C-Fe

0.1 g baking powder (BP) and 10.09 mmol glucose were mixed and dissolved in DIW along with the fermentation process at room temperature. Then, 110 mg $Ni(acac)_2$, 90 mg $Fe(acac)_3$ and 720 mg KBr were added and grinded. The sample was dissolved in a mixture of 25 mL ethanol and 5 mL DIW and stirred at room temperature until the the water was completely evaporated. The dried mixture was subsequently inserted into a muffle furnace and heated to 300 °C with a heating rate of 5 $°C{\cdot}min^{-1}$ for 12 h. After cooling down to room temperature, the powder underwent several wash processes with ethanol and DIW. The synthesis of C-NiFe followed the same method, except that prior fermentation was not utilized. Additionally, C-Ni and C-Fe were produced by using 110 mg $Ni(acac)_2$ and 90 mg $Fe(acac)_3$ as metal precursors, respectively, following the same procedure.

3 Results and discussion

During the synthesis process, we successfully prepared a series of C-

modified amorphous NiFe (*a*-NiFe) alloy catalysts using $Ni(acac)_2$ and $Fe(acac)_3$ as nickel and iron sources, glucose as carbon source and KBr as templating agent at a low reaction temperature of 300 °C for 12 h (Scheme 1). Based on the synthesis of *a*-NiFe alloy, we carried out carbon modification by adding glucose and it can be seen from Fig. S1 in the Electronic Supplementary Material (ESM) that the appearance of the material became fluffier after the addition of glucose, indicating that the addition of glucose not only introduces carbon dopant, but also helps to increase the specific surface area of the catalyst. Furthermore, after fermentation at room temperature, the appearance of the material is more fluffy (Fig. S2 in the ESM), resulting in a larger specific surface area of the catalyst.

The crystal structures of NiFe, C-NiFe and C-NiFe(BP) (Fig. 1(a)) were further investigated using X-ray diffraction (XRD). As can be seen from Fig. 1(a), NiFe, C-NiFe and C-NiFe(BP) all have only one broad peak and no other distinct peaks were scanned, indicating that the amorphous structure of the three catalysts [35]. The results show that carbon modification has no effect on the amorphous structure of NiFe alloys. In addition, the peaks of C-NiFe(BP), C-NiFe are shifted to a lower angle compared to NiFe and the shift angle of C-NiFe(BP) is larger. In order to investigate the structure of C, we subjected the glucose to the same processing steps as for the synthesis of C-NiFe(BP), which was then evaluated by XRD analysis. The XRD spectrum of C (Fig. S3 in the ESM) has a broad peak at about 25°, indicating an amorphous structure of the carbon. This indicates that the interlayer distance of the catalyst can be augmented following modification with carbon, which is conducive to the exposure of additional active sites and, consequently, an enhancement in the catalytic activity. The morphology of the synthesized catalysts were analyzed using scanning electron microscopy (SEM) and transmission electron microscopy (TEM). Based on SEM (Fig. 1(b)) and TEM (Fig. 1(d)) images, it can be seen that the C-NiFe(BP) shows the morphology of agglomerated bulk. From the SEM of NiFe and C-NiFe in Fig. S4 in the ESM, it can be seen that the agglomeration of NiFe is obvious and large and the nanosize of C-NiFe tends to become smaller and thinner. However, C-NiFe still has partial stacking compared to C-NiFe(BP), which is unfavourable for the exposure of active sites. The energy dispersive spectroscopy (EDS) (Fig. 1(c)) diagram clearly shows a uniform distribution of Ni, Fe and C, indicating effective modified carbon in the catalyst. By analysing the elemental content (Table S1 in the ESM), we can see that the nickel-iron ratio is close to 3:2, which is consistent with the nickel-iron ratio during the preparation process, proving that there is no large loss during catalyst synthesis. And the high carbon content confirms the successful synthesis and modification of carbon. Since the amorphous material has a disordered arrangement of atoms and no

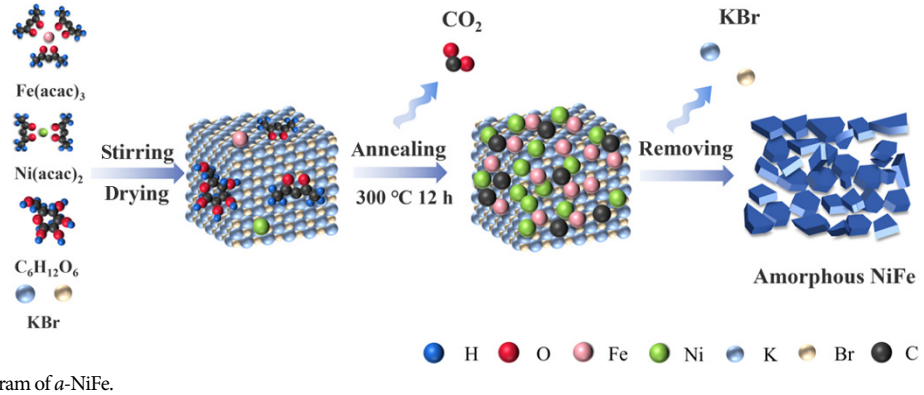

Scheme 1 Synthesis diagram of *a*-NiFe.

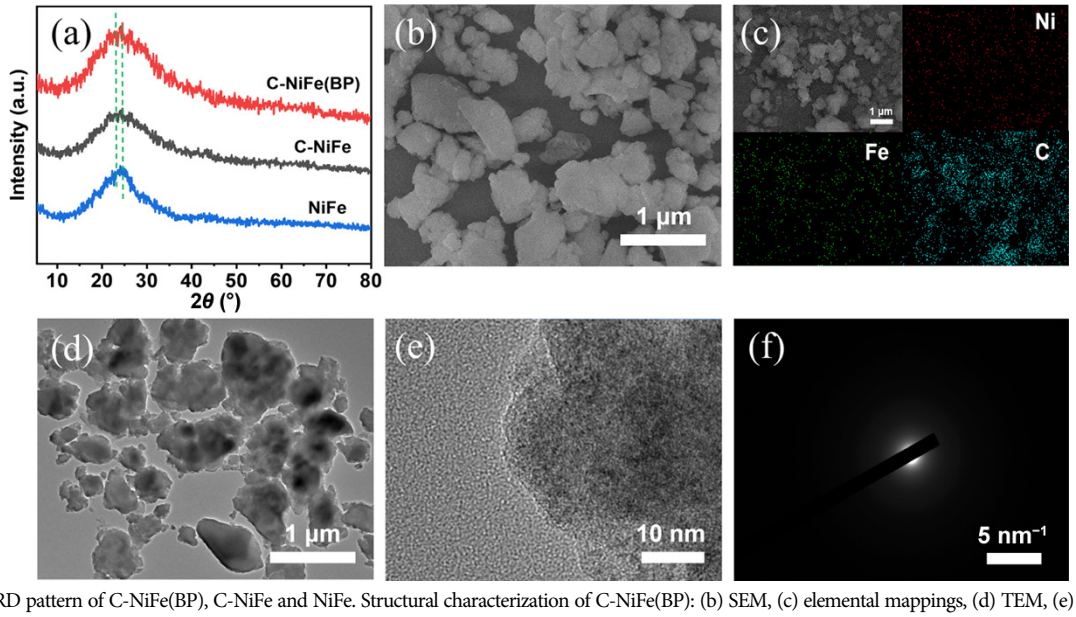

Figure 1 (a) XRD pattern of C-NiFe(BP), C-NiFe and NiFe. Structural characterization of C-NiFe(BP): (b) SEM, (c) elemental mappings, (d) TEM, (e) HRTEM and (f) SAED images.

obvious crystal structure, the amorphous nature of the material is proved by high resolution TEM (HRTEM) (Fig. 1(e)) [38, 39]. From the selected area electron diffraction (SAED) image (Fig. 1(f)), it can be found that C-NiFe(BP) has no obvious bright spots and clear rings, showing an indeterminate state, which also reflects the amorphous nature.

Raman spectroscopic studies in carbon material preparation are primarily concerned with characterising structural information and general interpretations corresponding to Raman peak positions characteristic of carbon materials, including D-peak and G-peak, are both characteristic Raman peaks of the C atomic crystal, so we also carried out Raman spectroscopy of the catalysts (Fig. 2(a)) and we can see that there is no carbon peak for NiFe, but there are D-peaks and G-peaks for C-NiFe (BP) and the D-peak signal is stronger than the G-peak, which further proves the amorphous nature of C. Subsequently, X-ray photoelectron spectroscopy (XPS) was used to analyze the chemical structure of the as-made catalysts. We comparatively analysed the XPS spectra of NiFe and C-NiFe(BP). As shown in Fig. 2(b), C, O, Ni and Fe are all exhibited in the full spectrum of NiFe and C-NiFe(BP). The element Ni is mainly present as Ni^{2+} in C-NiFe(BP), with its $2p_{3/2}$ peak at 856.9 eV and $2p_{1/2}$ peak at 874.8 eV (Fig. 2(c)) [39–48]. The results show that the characteristic peak position of Ni 2p is shifted by 1.1 eV towards higher bonding energy after carbon modification, manifesting that the C-modified can easily adjust the electronic structure of C-NiFe(BP) to optimize the adsorption of NiFe alloy nanoparticle and protons. Elemental Fe is also present mainly in two types: Fe^{2+} and Fe^{3+} (Fig. 2(d)). The Fe $2p_{3/2}$ and $2p_{1/2}$ peaks of Fe^{2+} are found at 710.8 and 723.9 eV, while Fe $2p_{3/2}$ and $2p_{1/2}$ for Fe^{3+} are located at 712.7 and 726.1 eV. Besides, the Fe 2p spectra indicate the presence of Fe^0, suggesting that the catalyst contains a small amount of iron and the two satellite peaks of Fe 2p at $2p_{3/2}$ and $2p_{1/2}$ corresponded to 715.2 and 732.1 eV, respectively [48]. As usual, there is a small shift in the position of the characteristic peak of Fe 2p, the inclusion of C in C-NiFe(BP) facilitates effective charge transfer through a simple adjustment of the electronic structure. Furthermore, the 1s peak of oxygen could be divided into two peaks, including the adsorbed H_2O and M–O peak (where M stands for transition metal) (Fig. 2(e)) [29, 49]. There is a slight change in the O 1s M–O peak in C-NiFe(BP) towards a low angle, indicative of robust interactions within the catalyst that facilitate expeditious charge transfer. We also analysed the C 1s spectra (Fig. 2(f)) of NiFe and C-NiFe(BP) and found that the C 1s spectra of NiFe and C-NiFe(BP), including the C–C, C–O and C=O. This suggests that the C-modified NiFe has a higher valence state and an intensified electronic interaction between NiFe and C.

In order to investigate the electrocatalytic performances of *a*-NiFe based catalysts, we tested the electrochemical properties using a three-electrode system in 1 M KOH. All the data of the tests can be referred to the reversible hydrogen electrode (RHE). To ensure the accuracy of the performance tests, all catalysts in the experiments were loaded on carbon sheets to ensure the mass loading with the same catalytically active components.

Linear scanning voltammetry (LSV) curves were obtained at a scan rate of 5 $mV \cdot s^{-1}$ within the potential range of 0–2 V vs. RHE. Various catalysts were synthesized by controlling the molar ratios of nickel and iron precursors. By controlling the molar ratios of NiFe to synthesise different catalysts, we electrochemically tested Ni:Fe = 3:1 (C-NiFe-1), Ni:Fe = 3:2 (C-NiFe-2), Ni:Fe = 3:3 (C-NiFe-3), Ni:Fe = 2:3 (C-NiFe-4). Among the catalysts, C-NiFe-2 shows the lowest overpotential@10 $mA \cdot cm^{-2}$ (η), which is only 224 mV (Fig. 3(a)) [39]. In addition, the scatter plots of the overpotential and Tafel slope plots are shown in Fig. 3(b) to compare the electrochemical performance of different catalyst ratios. The Tafel slope associates with the OER kinetics for C-NiFe-2 decreases to 50.49 $mV \cdot dec^{-1}$, while the respective Tafel slopes for C-NiFe-1, C-NiFe-3 and C-NiFe-4 are 57.01, 75.54 and 85.45 $mV \cdot dec^{-1}$. Electrochemical impedance spectroscopy (EIS) tests were carried out and the results are shown in Fig. 3(c). The electrochemical system is considered as an equivalent circuit with charge transfer resistance and solution resistance in series and the radius of curvature is proportional to the charge transfer resistance and inversely proportional to the charge transfer capacity. The radius is ordered as follows: C-NiFe-2 < C-NiFe-3 < C-NiFe-1 < C-NiFe-4. This suggests that C-NiFe-2 has a smaller charge transfer resistance in OER, which accelerates the rate of charge transfer in the OER

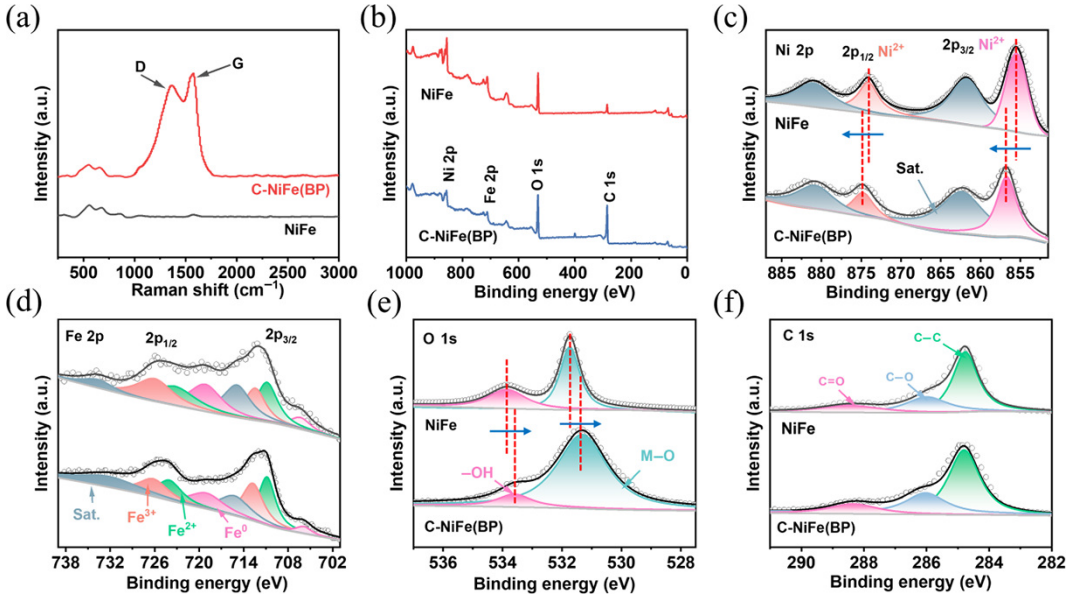

Figure 2 (a) Raman spectra of NiFe and C-NiFe(BP). XPS spectra of NiFe and C-NiFe(BP): (b) full spectrum and high-resolution XPS spectra of (c) Ni 2p, (d) Fe 2p, (e) O 1s and (f) C 1s.

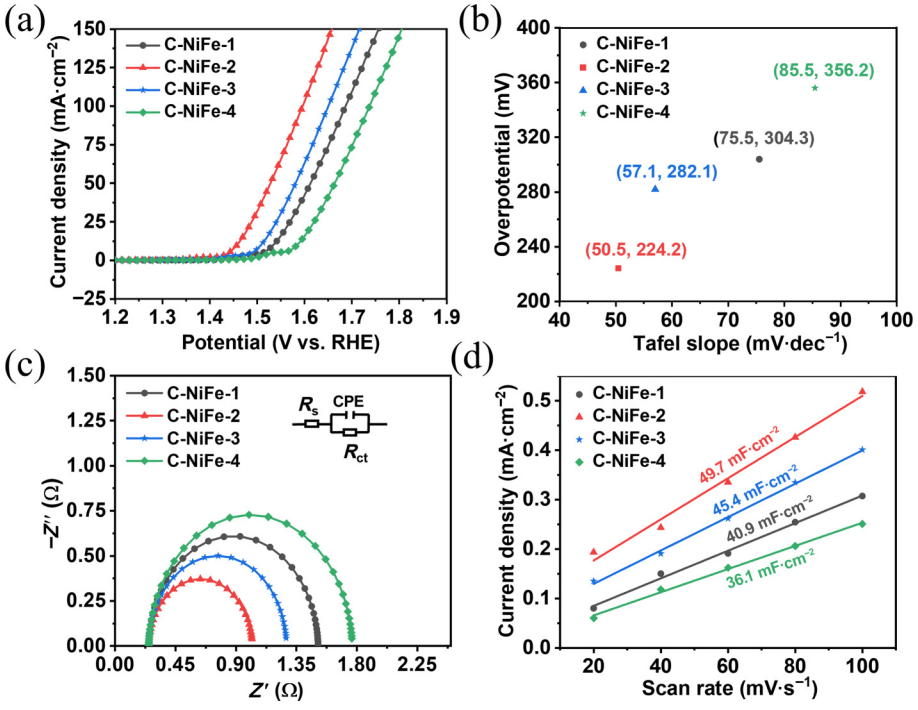

Figure 3 OER performances in 1 M KOH of the synthesized catalysts. (a) LSV curves of catalysts with the scan rate of 5 mV·s^{-1}, (b) the overpotentials and Tafel slopes, (c) Nyquist plots for the samples, and (d) C_{dl} values.

process and enhances the OER activity. The electrochemically active surface area (ECSA) represents the number of electrochemically active sites per unit area of the catalyst material. The double layer capacitance (C_{dl}) calculated from cyclic voltammetry (CV) curves at different scan rates is positively correlated with the ECSA and the value of C_{dl} can reflect the number of electrochemically active sites [37]. Scanning rates ranging from 20 to 100 mV·s^{-1} were conducted to test the CV (Fig. S5 in the ESM) curves. The C_{dl} value of 49.7 mF·cm^{-2} for C-NiFe-2 was higher than that of the other catalysts (45.4 mF·cm^{-2} for C-NiFe-3, 40.9 mF·cm^{-2} for C-NiFe-1, 36.1 mF·cm^{-2} for C-NiFe-4) (Fig. 3(d)), indicating that the properate ratio of Ni and Fe can generate more active sites.

The catalytic performance of the catalyst is affected by the quantity of modified carbon produced during carbonisation. Hence, after determining the optimal nickel-iron ratio in the synthesised material, the glucose amount was also regulated. The catalysts fabricated with different glucose addition (5.07 mmol (g-1), 7.57 mmol (g-2), 10.09 mmol (g-3), 12.62 mmol (g-4) and 15.14 mmol (g-5)) were tested for their electrochemical performance. When comparing the electrochemical test results, it is evident that the catalyst's performance is superior to the other dosages when the amount of glucose is controlled to be 10.09 mmol (Fig. S6 in the ESM). The η of g-3 is only 230.04 mV (Fig. S6(a) in the ESM), which is lower than that of the other catalysts. The Tafel slopes (Fig. S6(b) in the ESM) and the EIS (Fig. S6(c) in the ESM) data also demonstrate that g-3 has the superior OER performance.

In order to obtain a clearer understanding of the electrocatalytic performance of the catalysts and to demonstrate the superiority of the C-modified *a*-NiFe alloy, control samples were prepared by selecting the nickel-iron ratio with the best OER performance, which is 3:2. The control samples are C-modified amorphous monometallic (C-Ni, C-Fe), carbon-free amorphous bimetallic (NiFe), C-modified amorphous bimetallic (C-NiFe) and C-modified amorphous bimetallic (C-NiFe(BP)) after fermentation. As shown in Fig. 4(a), C-NiFe(BP) has the lowest η (219.7 mV), which is much lower than that of C-Ni (346.9 mV), C-Fe (376.1 mV), NiFe (261.7 mV) and C-NiFe (260.9 mV). The histogram of overpotentials in Fig. 4(b) is better illustrating that C-NiFe(BP) has the lowest overpotential. Tafel slopes obtained from the polarization curves show the kinetics of all samples, which are shown in Fig. 4(c). The Tafel slope for C-NiFe(BP) is the smallest with a value of 43.17 mV·dec^{-1}, which in C-Ni, C-Fe, NiFe, C-NiFe are 48.37, 51.6, 132.96 and 150.2 mV·dec^{-1}. The Tafel slopes have been calculated for each catalyst above the onset potential and are shown in Fig. 4(c). Unlike C-Ni, C-Fe catalysts, all NiFe-containing samples have a rate-determining value that reflects the characteristic Tafel slope of NiFe in the 1 M KOH concentration range (~ 50 mV·dec^{-1}). This further confirms that NiFe is the main OER catalyst in C-NiFe(BP) catalysts [50]. Figure 4(c) illustrates that the Tafel slope of the sample containing NiFe is approximately 50 mV·dec^{-1}, which substantiates the assertion that the rate-determining step of the catalyst is the generation of oxygen from *O [51]. The large difference in Tafel slopes suggests that carbon modified-induced changes in electronic structure play a crucial role in facilitating the promotion of catalysts in OER kinetics. The electrochemical test results demonstrate that bimetallic or multimetallic catalysts typically display enhanced catalytic activity relative to monometallic catalysts. This phenomenon can be attributed to the interactions between different metal atoms, which give rise to a synergistic interaction between the two nearest metal sites, thereby improving the catalytic activity. The electrochemical performance of C-NiFe(BP) offers great advantages over the published literature (refer to Table S3 in the ESM). Overall the C-NiFe(BP) catalyst exceeds most state-of-the-art NiFe-based catalysts. In addition, C-NiFe(BP) also has the fastest electron transport capability within the catalyst interface as observed by EIS. The smaller circle diameter confirms the lower resistance interfacial kinetic pathway achieved on the C-NiFe(BP) surface (Fig. 4(d)). CV

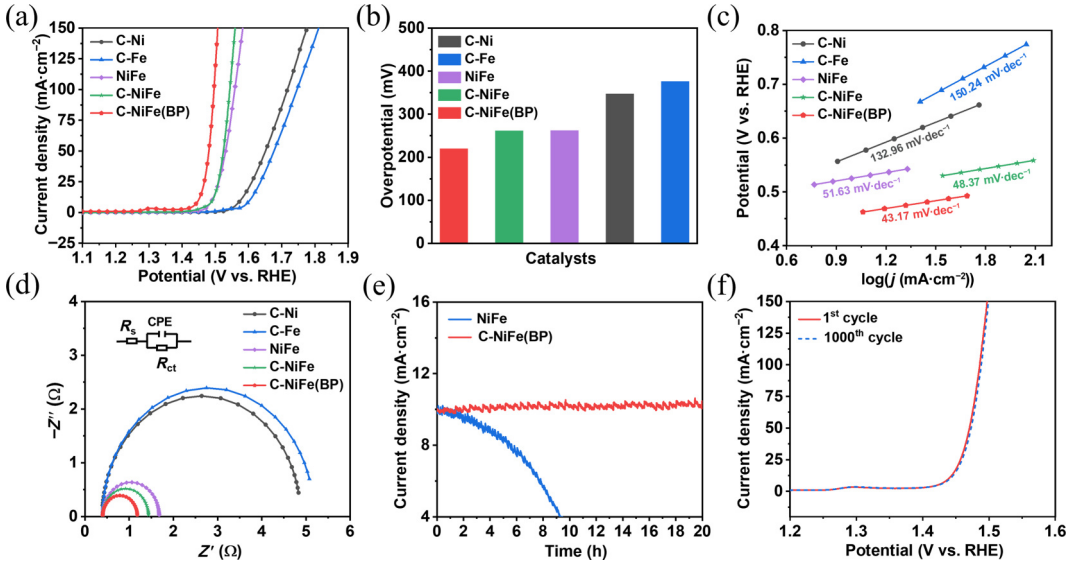

Figure 4 OER performance of C-Ni, C-Fe, NiFe, C-NiFe and C-NiFe(BP) conducted in 1 M KOH. (a) LSV curves of catalysts with the scan rate of 5 mV·s^{-1}, (b) the overpotentials, (c) Tafel slopes of different catalysts, (d) Nyquist plots for the samples, (e) polarization data for NiFe and C-NiFe(BP) catalysts for 20 h long term durability test, and (f) polarization data for C-NiFe(BP).

was carried out in the non-Faraday potential range to calculate the C_{dl} of the active materials, which was proportionally related to their ECSA. As can be seen from Fig. S8 in the ESM, C-NiFe(BP) have a higher C_{dl} value (ECSA = 51.97 mF·cm^{-2}). The turnover frequency (TOF) was calculated to provide insight into the intrinsic catalytic activity of the electrocatalysts (refer to Table S4 in the ESM). Among the synthesised catalysts, C-NiFe(BP) exhibited the highest TOF value (1.16 S^{-1}), surpassing C-Ni (0.34 S^{-1}), C-Fe (0.13 S^{-1}), NiFe (0.49 S^{-1}) and C-NiFe (0.88 S^{-1}). This suggests that C-NiFe(BP) has more active sites, which enhances its OER performance. The results indicate that the designed C-NiFe(BP) catalyst exhibits excellent OER performance, suggesting that the carbon-modified *a*-NiFe alloys are rich in active sites and have appropriate electronic structure. Long-term operational stability is directly related to the structural stability of the catalysts and can confirm the reliable performance of the catalysts for industrial target applications. For C-NiFe(BP), the catalytic current density can be maintained for at least 20 h without significant decrease (Fig. 4(e)), but without carbon modified, the catalytic activity decays at a very fast rate, indicating that carbon modified can improve the stability of *a*-NiFe alloy. Furthermore, EDS characterisation of the catalysts following the stability tests revealed that there was only a minimal amount of Ni and Fe content transferred compared to that observed prior to the reaction. This finding substantiates the stability of the catalyst structure. Figure 4(f) shows the OER polarisation LSV curves of C-NiFe(BP) before and after 1000 CV cycles. Only a negligible potential shift at 10 mA·cm^{-2} can be observed, which indicates that C-NiFe(BP) has a robust structural stability after repeated electrocatalytic processes. To better demonstrate the structural stability of the synthesised catalysts, we analyzed the XPS of before and after C-NiFe(BP) reaction (Fig. S9 in the ESM). The results show that no significant changes occurred in the positions of the main peaks of Ni 2p and Fe 2p (Figs. S9(b) and S9(c) in the ESM), indicating that the chemical structure of the main structure of C-NiFe(BP) was not disturbed after the reaction. In addition, consistent with the stability test results, it is well demonstrated that the catalyst is able to maintain stability over a long period of time during the reaction process.

4 Conclusions

In summary, we synthesized a C-modified *a*-NiFe alloy via a one-step annealing method using room temperature fermentation with glucose as the carbon source. C-modified towards the amorphous alloy can improve the stability of the catalyst and the excellent OER activity can be maintained after 20 h stability test and 1000 cycles' CV test. Meanwhile, the comparison of the XPS peaks of Ni and Fe before and after the reaction showed no obvious shift, further demonstrating the superior structural stability of the catalyst. Notably, the appearance of the catalyst was significantly fluffy after fermentation and the peak of C-NiFe(BP) could be seen to be shifted to a lower angle when analysed by XRD, which proved that carbon modification could expand the interlayer of the catalyst, this greatly increased the specific surface area of the catalyst and exposed more active sites, which further improved the catalytic performance. Furthermore, C-NiFe(BP) demonstrates exceptional OER performance, achieving a current density of 10 mA·cm^{-2} with a remarkably low overpotential of 219.7 mV. Notably, it exhibits a Tafel slope of 43.17 mV·dec^{-1} and a C_{dl} value of 51.97 mF·cm^{-1}. This work provides a new idea on stable amorphous bi-metal alloy synthesis with carbon modified to increase the specific surface area of catalysts with more active sites, providing insights into the design of amorphous alloys with high stability and OER properties.

Electronic Supplementary Material: Supplementary material (test method, Figs. S1–S9 and Tables S1–S4) is available in the online version of this article at https://doi.org/10.26599/NR.2025.94907019.

Data availability

All data needed to support the conclusions in the paper arepresented in the manuscript and/or the Electronic Supplementary Material. Additional data related to this paper may be requested from the corresponding author upon request.

Acknowledgements

This work is supported by the Young Taishan Scholarship Project

of Shandong Province (No. tsqn201909115), Shandong Province Key Research and Development Plan (Major Scientific and Technological Innovation Project) (No. 2023CXGC010303), 2023 Province's New and Old Kinetic Energy Conversion of Major Industrial Research Projects, National Funded Postdoctoral Program of China (No. GZC20231195), Qingdao Postdoctoral Funding Project (No. QDBSH20240102087). The authors extend their appreciation to Taif University, Saudi Arabia, for supporting this work through project (No. TU-DSPP-2024-01).

Declaration of competing interest

All the contributing authors report no conflict of interests in this work.

Author contribution statement

Y. Z. Q.: Experimental design, data curation, software, methodology, writing manuscript. L. P.: Data curation, software, methodology, validation, writing manuscript. H. M. J.: Data curation, software, methodology. M. A. A.: Project administration, methodology, funding acquisition. J. J. L.: Supervision, experimental design, project administration, funding acquisition, writing manuscript. All the authors have approved the final manuscript.

Use of AI statement

None.

References

[1] Cao, Q.; Cheng, Z. Y.; Dai, J. J.; Sun, T. X.; Li, G. X.; Zhao, L. L.; Yu, J. Y.; Zhou, W. J.; Lin, J. J. Enhanced hydrogen evolution reaction over co nanoparticles embedded N-doped carbon nanotubes electrocatalyst with Zn as an accelerant. *Small* **2022**, *18*, 2204827.

[2] Yu, Z. Y.; Duan, Y.; Feng, X. Y.; Yu, X. X.; Gao, M. R.; Yu, S. H. Clean and affordable hydrogen fuel from alkaline water splitting: Past, recent progress, and future prospects. *Adv. Mater.* **2021**, *33*, 2007100.

[3] You, H. H.; Wu, D. S.; Si, D. H.; Cao, M. N.; Sun, F. F.; Zhang, H.; Wang, H. M.; Liu, T. F.; Cao, R. Monolayer NiIr-layered double hydroxide as a long-lived efficient oxygen evolution catalyst for seawater splitting. *J. Am. Chem. Soc.* **2022**, *144*, 9254–9263.

[4] Niu, F. J.; Wang, D. G.; Li, F.; Liu, Y. M.; Shen, S. H.; Meyer, T. J. Hybrid photoelectrochemical water splitting systems: From interface design to system assembly. *Adv. Energy Mater.* **2020**, *10*, 1900399.

[5] Son, S.; Koo, B.; Chai, H.; Tran, H. V. H.; Pandit, S.; Jung, S. P. Comparison of hydrogen production and system performance in a microbial electrolysis cell containing cathodes made of non-platinum catalysts and binders. *J. Water Process Eng.* **2021**, *40*, 101844.

[6] Liu, H.; Shen, W.; Jin, H. Y.; Xu, J.; Xi, P. X.; Dong, J. C.; Zheng, Y.; Qiao, S. Z. High-performance alkaline seawater electrolysis with anomalous chloride promoted oxygen evolution reaction. *Angew. Chem., Int. Ed.* **2023**, *62*, e202311674.

[7] Gao, C.; Kong, L. H.; Pan, L.; Li, D. X.; Lin, J. J. A novel sacrificial solvent method to synthesize self-supporting Co_9S_8/Ni_3S_2 heterostructure catalyst for efficient oxygen evolution reaction. *J. Colloid Interface Sci.* **2023**, *652*, 1756–1763.

[8] Kumar, A.; Purkayastha, S. K.; Guha, A. K.; Das, M. R.; Deka, S. Designing nanoarchitecture of nicu dealloyed nanoparticles on hierarchical Co nanosheets for alkaline overall water splitting at low cell voltage. *ACS Catal.* **2023**, *13*, 10615–10626.

[9] Li, M.; Zhu, H. Y.; Yuan, Q.; Li, T. Y.; Wang, M. M.; Zhang, P.; Zhao, Y. L.; Qin, D. L.; Guo, W. Y.; Liu, B. et al. Proximity electronic effect of Ni/Co diatomic sites for synergistic promotion of electrocatalytic oxygen reduction and hydrogen evolution. *Adv. Funct. Mater.* **2023**, *33*, 2210867.

[10] Gong, Z. C.; Liu, R.; Gong, H. S.; Ye, G. L.; Liu, J. J.; Dong, J. C.; Liao, J. W.; Yan, M. M.; Liu, J. B.; Huang, K. et al. Constructing a graphene-encapsulated amorphous/crystalline heterophase NiFe alloy by microwave thermal shock for boosting the oxygen evolution reaction. *ACS Catal.* **2021**, *11*, 12284–12292.

[11] Zhuang, L. Z.; Jia, Y.; Liu, H. L.; Li, Z. H.; Li, M. R.; Zhang, L. Z.; Wang, X.; Yang, D. J.; Zhu, Z. H.; Yao, X. D. Sulfur-modified oxygen vacancies in iron-cobalt oxide nanosheets: Enabling extremely high activity of the oxygen evolution reaction to achieve the industrial water splitting benchmark. *Angew. Chem., Int. Ed.* **2020**, *59*, 14664–14670.

[12] Sun, J.; Xue, H.; Guo, N. K.; Song, T. S.; Hao, Y. R.; Sun, J. W.; Zhang, J. W.; Wang, Q. Synergetic metal defect and surface chemical reconstruction into $NiCo_2S_4$/ZnS heterojunction to achieve outstanding oxygen evolution performance. *Angew. Chem., Int. Ed.* **2021**, *60*, 19435–19441.

[13] Wang, X. L.; Ma, R. G.; Li, S. L.; Xu, M. M.; Liu, L. J.; Feng, Y. H.; Thomas, T.; Yang, M. H.; Wang, J. C. *In situ* electrochemical oxyanion steering of water oxidation electrocatalysts for optimized activity and stability. *Adv. Energy Mater.* **2023**, *13*, 2300765.

[14] Cheng, Z. Y.; Qu, C.; Gao, C.; Kong, L. H.; Yin, P. G.; Lin, J. J. Promoting surface reconstruction of low-cost stainless steel catalyst for efficient oxygen evolution reaction. *Chem.—Eur. J.* **2023**, *29*, e202300741.

[15] Ko, Y. J.; Han, M. H.; Kim, H.; Kim, J. Y.; Lee, W. H.; Kim, J.; Kwak, J. Y.; Kim, C. H.; Park, T. E.; Yu, S. H. et al. Unraveling Ni-Fe 2D nanostructure with enhanced oxygen evolution via *in situ* and *operando* spectroscopies. *Chem Catal.* **2022**, *2*, 2312–2327.

[16] Liu, C. C.; Han, Y.; Yao, L. B.; Liang, L. M.; He, J. Y.; Hao, Q. Y.; Zhang, J.; Li, Y.; Liu, H. Engineering bimetallic NiFe-based hydroxides/selenides heterostructure nanosheet arrays for highly-efficient oxygen evolution reaction. *Small* **2021**, *17*, 2007334.

[17] Fan, K.; Chen, H.; Ji, Y. F.; Huang, H.; Claesson, P. M.; Daniel, Q.; Philippe, B.; Rensmo, H.; Li, F. S.; Luo, Y. et al. Nickel-vanadium monolayer double hydroxide for efficient electrochemical water oxidation. *Nat. Commun.* **2016**, *7*, 11981.

[18] Jing, Z. X.; Zhao, Q. Y.; Zheng, D. H.; Xu, H. Z.; Sun, L.; Geng, J. H.; Zhou, Q. N.; Lin, J. J. Engineering unique $Fe(Se_xS_{1-x})_2$ nanorod bundles for boosting oxygen evolution reaction. *Chem. Eng. J.* **2021**, *418*, 129426.

[19] Magnier, L.; Cossard, G.; Martin, V.; Pascal, C.; Roche, V.; Sibert, E.; Shchedrina, I.; Bousquet, R.; Parry, V.; Chatenet, M. Fe-Ni-based alloys as highly active and low-cost oxygen evolution reaction catalyst in alkaline media. *Nat. Mater.* **2024**, *23*, 252–261.

[20] Wang, K. X.; Wang, X. Y.; Li, Z. J.; Yang, B.; Ling, M.; Gao, X.; Lu, J. G.; Shi, Q. R.; Lei, L. C.; Wu, G. et al. Designing 3d dual transition metal electrocatalysts for oxygen evolution reaction in alkaline electrolyte: Beyond oxides. *Nano Energy* **2020**, *77*, 105162.

[21] Cai, J. S.; Jin, J.; Fan, Z. D.; Li, C.; Shi, Z. X.; Sun, J. Y.; Liu, Z. F. 3D printing of a V_8C_7-Vo_2 bifunctional scaffold as an effective polysulfide immobilizer and lithium stabilizer for Li-S batteries. *Adv. Mater.* **2020**, *32*, 2005967.

[22] Yang, X.; Chen, Q. Q.; Wang, C. J.; Hou, C. C.; Chen, Y. Substrate participation ultrafast synthesis of amorphous NiFe nanosheets on iron foam at room temperature toward highly efficient oxygen evolution reaction. *J. Energy Chem.* **2019**, *35*, 197–203.

[23] Viswanathan, P.; Kim, K. *In situ* surface restructuring of amorphous Ni-doped CoMo phosphate-based three-dimensional networked nanosheets: Highly efficient and durable electrocatalyst for overall alkaline water splitting. *ACS Appl. Mater. Interfaces* **2023**, *15*, 16571–16583.

[24] Sun, L.; Gao, M.Y.; Jing, Z. X.; Cheng, Z. Y.; Zheng, D. H.; Xu, H. Z.; Zhou, Q. N.; Lin, J. J. 1 T-phase enriched P doped WS_2

nanosphere for highly efficient electrochemical hydrogen evolution reaction. *Chem. Eng. J.* **2022**, *429*, 132187.
[25] Wu, G.; Zheng, X. S.; Cui, P. X.; Jiang, H. Y.; Wang, X. Q.; Qu, Y. T.; Chen, W. X.; Lin, Y.; Li, H.; Han, X. et al. A general synthesis approach for amorphous noble metal nanosheets. *Nat. Commun.* **2019**, *10*, 4855.
[26] Yoon, Y.; Yan, B.; Surendranath, Y. Suppressing ion transfer enables versatile measurements of electrochemical surface area for intrinsic activity comparisons. *J. Am. Chem. Soc.* **2018**, *140*, 2397–2400.
[27] Chen, G.; Zhu, Y. P.; Chen, H. M.; Hu, Z. W.; Hung, S. F.; Ma, N. N.; Dai, J.; Lin, H. J.; Chen, C. T.; Zhou, W. et al. An amorphous nickel-iron-based electrocatalyst with unusual local structures for ultrafast oxygen evolution reaction. *Adv. Mater.* **2019**, *31*, 1900883.
[28] Sun, R. B.; Gao, J. Y.; Wu, G.; Liu, P. G.; Guo, W. X.; Zhou, H.; Ge, J. J.; Hu, Y. M.; Xue, Z. G.; Li, H. et al. Amorphous metal oxide nanosheets featuring reversible structure transformations as sodium-ion battery anodes. *Cell Rep. Phys. Sci.* **2020**, *1*, 100118.
[29] Wu, D. L.; Liu, B.; Li, R. D.; Chen, D.; Zeng, W. H.; Zhao, H. Y.; Yao, Y. T.; Qin, R.; Yu, J.; Chen, L. et al. Fe-regulated amorphous-crystal Ni(Fe)P_2 nanosheets coupled with Ru powerfully drive seawater splitting at large current density. *Small* **2023**, *19*, 2300030.
[30] Hou, X. B.; Han, Z. K.; Xu, X. J.; Sarker, D.; Zhou, J.; Wu, M.; Liu, Z. C.; Huang, M. H.; Jiang, H. Q. Controllable amorphization engineering on bimetallic metal-organic frameworks for ultrafast oxygen evolution reaction. *Chem. Eng. J.* **2021**, *418*, 129330.
[31] Li, X. J.; Zhang, H. K.; Hu, Q.; Zhou, W. L.; Shao, J. X.; Jiang, X. X.; Feng, C.; Yang, H. P.; He, C. X. Amorphous NiFe oxide-based nanoreactors for efficient electrocatalytic water oxidation. *Angew. Chem., Int. Ed.* **2023**, *62*, e202300478.
[32] Wang, H. T.; Sun, J. K.; Wang, J. L.; Jiang, L. P.; Liu, H. F. Green synthesis of nitrogen and fluorine co-doped porous carbons from sustainable coconut shells as an advanced synergistic electrocatalyst for oxygen reduction. *J. Mater. Res. Technol.* **2021**, *13*, 962–970.
[33] Yang, C. M.; Zhang, L.; Lu, Y. X.; Zou, Y. Q.; Wang, S. Y. Designing efficient catalysts for electrocatalytic organic synthesis: From electronic structure to adsorption behavior. *Matter* **2024**, *7*, 456–474.
[34] Zhao, Y. Y.; Zhang, Y. L.; Wang, Y.; Cao, D. X.; Sun, X.; Zhu, H. L. Versatile zero- to three-dimensional carbon for electrochemical energy storage. *Carbon Energy* **2021**, *3*, 895–915.
[35] Sun, Y. W.; Wang, H. L.; Wei, W. R.; Zheng, Y. L.; Tao, L.; Wang, Y. X.; Huang, M. H.; Shi, J.; Shi, Z. C.; Mitlin, D. Sulfur-rich graphene nanoboxes with ultra-high potassiation capacity at fast charge: Storage mechanisms and device performance. *ACS Nano* **2021**, *15*, 1652–1665.
[36] Zhang, M. T.; Li, H.; Chen, J. X.; Ma, F. X.; Zhen, L.; Wen, Z. H.; Xu, C. Y. Transition metal (Co, Ni, Fe, Cu) single-atom catalysts anchored on 3D nitrogen-doped porous carbon nanosheets as efficient oxygen reduction electrocatalysts for Zn-Air battery. *Small* **2022**, *18*, 2202476.
[37] Song, Y.; Liu, T. Y.; Li, M. Y.; Yao, B.; Kou, T. Y.; Feng, D. Y.; Wang, F. X.; Tong, Y. X.; Liu, X. X.; Li, Y. Engineering of mesoscale pores in balancing mass loading and rate capability of hematite films for electrochemical capacitors. *Adv. Energy Mater.* **2018**, *8*, 1801784.
[38] Xiao, M.; Qi, W. Q.; Jia, S. H.; Pang, M. T.; Shi, F. C.; Mao, H. High-performance removal of tetracycline enabled by Fe^0 nanoparticles supported on carbon@ZIF-8. *Chem. Res. Chin. Univ.* **2022**, *38*, 1349–1355.
[39] Li, R. L.; Rao, D. W.; Zhou, J. B.; Wu, G.; Wang, G. Z.; Zhu, Z. X.; Han, X.; Sun, R. B.; Li, H.; Wang, C. et al. Amorphization-induced surface electronic states modulation of cobaltous oxide nanosheets for lithium-sulfur batteries. *Nat. Commun.* **2021**, *12*, 3102.
[40] Wang, W. C.; He, T. O.; Yang, X. L.; Liu, Y. M.; Wang, C. Q.; Li, J.; Xiao, A. D.; Zhang, K.; Shi, X. T.; Jin, M. S. General synthesis of amorphous PdM (M = Cu, Fe, Co, Ni) alloy nanowires for boosting HCOOH dehydrogenation. *Nano Lett.* **2021**, *21*, 3458–3464.
[41] Bai, Y. K.; Wu, Y.; Zhou, X. C.; Ye, Y. F.; Nie, K. Q.; Wang, J. O.; Xie, M.; Zhang, Z. X.; Liu, Z. J.; Cheng, T. et al. Promoting nickel oxidation state transitions in single-layer NiFeB hydroxide nanosheets for efficient oxygen evolution. *Nat. Commun.* **2022**, *13*, 6094.
[42] Jing, Z. X.; Zhao, Q. Y.; Zheng, D. H.; Sun, L.; Geng, J. H.; Zhou, Q. N.; Lin, J. J. Nickel-doped pyrrhotite iron sulfide nanosheets as a highly efficient electrocatalyst for water splitting. *J. Mater. Chem. A* **2020**, *8*, 20323–20330.
[43] Jiang, S. S.; Zhu, L.; Yang, Z. Z.; Wang, Y. G. Morphological-modulated FeNi-based amorphous alloys as efficient alkaline water splitting electrocatalysts. *Electrochim. Acta* **2021**, *389*, 138756.
[44] Lin, Y. P.; Wang, H.; Peng, C. K.; Bu, L. M.; Chiang, C. L.; Tian, K.; Zhao, Y.; Zhao, J. Q.; Lin, Y. G.; Lee, J. M. et al. Co-induced electronic optimization of hierarchical NiFe LDH for oxygen evolution. *Small* **2020**, *16*, 2002426.
[45] Wilhelm, M.; Bastos, A.; Neves, C.; Martins, R.; Tedim, J. Ni-Fe layered double hydroxides for oxygen evolution reaction: Impact of Ni/Fe ratio and crystallinity. *Mater. Des.* **2021**, *212*, 110188.
[46] Cheng, Z. Y.; Gao, M. Y.; Sun, L.; Zheng, D. H.; Xu, H. Z.; Kong, L. H.; Gao, C.; Yu, H. Z.; Lin, J. J. FeSe/$FeSe_2$ heterostructure as a low-cost and high-performance electrocatalyst for oxygen evolution reaction. *ChemElectroChem* **2022**, *9*, e202200399.
[47] Ehsan, M. A.; Khan, A.; Hakeem, A. S. Binary CoNi and ternary FeCoNi alloy thin films as high-performance and stable electrocatalysts for oxygen evolution reaction. *ACS Appl. Energy Mater.* **2023**, *6*, 9556–9567.
[48] Zhou, F. L.; Gan, M. X.; Yan, D. F.; Chen, X. L.; Peng, X. Hydrogen-rich pyrolysis from Ni-Fe heterometallic Schiff base centrosymmetric cluster facilitates NiFe alloy for efficient OER electrocatalysts. *Small* **2023**, *19*, 2208276.
[49] Yu, L.; Zhou, H. Q.; Sun, J. Y.; Qin, F.; Yu, F.; Bao, J. M.; Yu, Y.; Chen, S.; Ren, Z. F. Cu nanowires shelled with NiFe layered double hydroxide nanosheets as bifunctional electrocatalysts for overall water splitting. *Energy Environ. Sci.* **2017**, *10*, 1820–1827.
[50] Singha Roy, S.; Madhu, R.; Karmakar, A.; Kundu, S. From theory to practice: A critical and comparative assessment of tafel slope analysis techniques in electrocatalytic water splitting. *ACS Mater. Lett.* **2024**, *6*, 3112–3123.
[51] Marshall, A. T.; Vaisson-Béthune, L. Avoid the quasi-equilibrium assumption when evaluating the electrocatalytic oxygen evolution reaction mechanism by Tafel slope analysis. *Electrochem. Commun.* **2015**, *61*, 23–26.